Nano Energy 153 (2026) 111919

Contents lists available at ScienceDirect

Nano Energy

journal homepage: www.elsevier.com/locate/nanoen

Full paper

Tailoring electrolyte solvation structure to enhance rate capability, cycle life, and safety in Prussian-blue-based sodium-ion battery

Thanh-Nhan Tran [a,*], Vadim Shipitsyn [b], Huong T.D. Nguyen [c], Yaobin Xu [e], Peiyuan Gao [f], Yuxin Yang [g], Changyu Yuan [h], Khanh T. Nguyen [c], Kha Minh Le [a], Thuy-Dung Tran [a], An L. Phan [a], Brett L. Lucht [g], Yan Yao [h], Tao Li [c,d], Chongmin Wang [e], Lin Ma [b,*], Phung M.L. Le [a,*]

[a] Energy and Environmental Directorate, Pacific Northwest National Laboratory, Richland, WA 99354, USA
[b] Department of Applied Physical Sciences, University of North Carolina at Chapel Hill, Chapel Hill, NC 27514, USA
[c] Department of Chemistry, Virginia Tech, Blacksburg, VA 24061, USA
[d] Chemistry and Material Science Group, X-ray Science Division, Argonne National Laboratory, Lemont, IL 60439, USA
[e] Environmental and Molecular Sciences Laboratory, Pacific Northwest National Laboratory, Richland, WA 99354, USA
[f] Physical and Computational Sciences Directorate, Pacific Northwest National Laboratory, Richland, WA 99354, USA
[g] Department of Chemistry, University of Rhode Island, Kingston, RI 02881, USA
[h] Materials Science and Engineering Program and Texas Center for Superconductivity at the University of Houston, University of Houston, Houston, TX 77204, USA

ARTICLE INFO

Keywords:
LHCE
Prussian Blue
Anion-derived SEI/CEI
High-rate cycling
Accelerating rate calorimetry

ABSTRACT

Prussian-blue (PB) cathodes paired with hard carbon (HC) anodes are promising for low-cost sodium-ion batteries (SIBs), but practical deployment is limited by rapid degradation at high charge/discharge rates and safety issues arising from electrolyte-driven interfacial reactions. Here, we develop a localized high-concentration electrolyte (LHCE) based on NaFSI in diglyme with a non-solvating fluorinated diluent (TTE) and benchmark against a diluted ether electrolyte (DE), a high-concentration ether electrolyte (HCE). HC|PB full cells with LHCE deliver outstanding high-rate durability, sustaining 80% capacity for ~1200 cycles at 2 C and strongly outperforming HCE and DE. Raman, Small-angle X-ray scattering (SAXS), and *ab initio* molecular dynamics (AIMD) reveal that LHCE increases anion involvement in the Na^+ primary solvation sheath (higher contact ion pairs and aggregates fraction), which shifts interphase formation toward anion-derived products. Post-mortem analyses show that LHCE forms thinner, more inorganic FSI-derived SEI/CEI on both electrodes, suppressing parasitic reactions, mitigating PB degradation and Fe migration, and reducing polarization growth under high-rate operation. In multilayer pouch cells, LHCE retains 82% capacity after 500 cycles with stable Coulombic efficiency (~99.3%), generates negligible gas (0.26 mL/Ah), and improves thermal safety by delaying exothermic onset in accelerating rate calorimetry relative to conventional carbonated-based electrolyte (CBE). Overall, solvation-structure engineering via LHCE provides a practical pathway to simultaneously enhance rate capability, cycle life, and safety in PB-based SIBs.

1. Introduction

Sodium-ion batteries (SIBs) are emerging as a compelling complement to lithium-ion technology for large-scale energy storage because sodium is abundant and low cost, and SIB manufacturing can leverage existing lithium-ion production infrastructure. Prussian blue and Prussian blue analogues (PB/PBAs) are especially attractive cathodes for SIBs due to their low-temperature synthesis, earth-abundant elements, and an open-framework structure that supports fast Na^+ transport with small volume change during cycling [1,2]. Despite rapid progress in PBA materials engineering [3,4], practical full-cell performance particularly at high charge/discharge rates and under safety-relevant abuse conditions remains strongly limited by electrolyte-driven interfacial instability rather than bulk electrode kinetics alone [5–7].

In PB|hard carbon (HC) full cells, the dominant degradation pathways at elevated rate are typically interfacial: sluggish Na^+ desolvation/

* Corresponding authors.
E-mail addresses: ttnhan@pnnl.gov (T.-N. Tran), L.ma@unc.edu (L. Ma), phung.le@pnnl.gov (P.M.L. Le).

https://doi.org/10.1016/j.nanoen.2026.111919
Received 1 March 2026; Received in revised form 23 March 2026; Accepted 26 March 2026
Available online 27 March 2026

charge transfer, continuous electrolyte decomposition, CEI/SEI thickening, and loss of cyclable Na through parasitic reactions [8–10]. In addition, PB/PBA cathodes can suffer from interfacial side reactions and dissolution-related degradation, which can further trigger cathode–anode cross-talk and accelerate impedance rise and capacity decay [11]. On the anode side, hard carbon is well known to form a thick and chemically complex SEI in conventional carbonate electrolytes, which lowers initial Coulombic efficiency, increases polarization, and degrades rate capability issues that can be aggravated as current density increases [5,8]. These challenges are not independent: the primary solvation sheath of Na^+ controls which species reach the electrode surface and decompose first, thereby governing the chemistry and morphology of the SEI/CEI and ultimately the rate capability, cycle life, and safety of the full cell [12].

Electrolyte design strategies that increase anion participation in the Na^+ solvation environment can shift interphase formation away from solvent-derived organic products toward more inorganic components (e.g., NaF and sulfur/nitrogen-containing species), which are frequently associated with more passivating interphases and reduced parasitic reactions [12]. High-concentration electrolytes (HCEs) naturally promote anion-rich solvation with high fractions of contact ion pairs and aggregates (CIP/AGG), but their high viscosity and reduced wettability can penalize transport and high-rate performance. Localized high-concentration electrolytes (LHCEs) address this trade-off by introducing non-solvating diluents that lower viscosity while largely preserving the anion-rich local coordination environment [13–15]. Recent work has shown glyme-based LHCE concepts can improve the stability of Na-ion battery materials and interphase, highlighting their promise for high-performance SIBs [16]. However, for PB|HC full cells, an LHCE strategy that simultaneously delivers high-rate durability, suppressed gassing, and improved thermal safety while providing clear solvation-to-interphase mechanistic evidence remains underdeveloped.

In this work, we tailor Na^+ solvation using an ether-based LHCE composed of NaFSI in diglyme (DI) with a fluorinated diluent 1,1,2,2-tetrafluoroethyl 2,2,3,3-tetrafluoropropylether (TTE) and compare it against a diluted ether electrolyte (DE) 1 M $NaPF_6$ in DI and a conventional carbonate-based electrolyte benchmark (CBE) 1 M $NaPF_6$ in EC/EMC (3/7, wt%). Our central hypothesis is that an LHCE that increases anion involvement in the Na^+ solvation sheath will promote anion-derived interphases on both HC and PB, which suppress continuous parasitic reactions and PB degradation/cross-talk, and reduce polarization growth under high-rate operation, thereby improving cycle life and safety (reduced gas generation and enhanced thermal stability). We first quantify solvation structure and nanoscale organization (DFT screening, Raman, SAXS, and AIMD), then connect these solvation features to interphase chemistry and thickness (XPS, HR-TEM, and ToF-SIMS) and finally validate practical performance across low-to-high rate cycling and in multilayer pouch cells, including leakage current, gas evolution, and accelerating rate calorimetry.

2. Results and discussion

2.1. Electrolyte design principle and solvation structures

Choosing an electrolyte requires balancing electrochemical stability and ion-solvation capability. As an initial screening tool, the energies of the highest occupied molecular orbital (HOMO) and lowest unoccupied molecular orbital (LUMO) provide qualitative insight into oxidative and reductive susceptibility. As shown in Figure S1a, diglyme (DI) exhibits a relatively high LUMO (2.27 eV), suggesting favorable reductive tolerance, while the fluorinated diluent TTE shows a comparable LUMO (2.21 eV) but a much lower HOMO (−10.7 eV) than DI and carbonate solvents (e.g., EC and EMC), indicating stronger oxidative tolerance. These results motivate combining DI (as the coordinating solvent) with TTE (as a non-solvating, oxidation-resistant diluent) to widen the practical stability margin and suppress parasitic reactions in LHCE relative to the DE. In addition, cation–solvent interaction strength governs solvation structure. Electrostatic potential (ESP) mapping provides a useful descriptor for solvent screening, where the minimum ESP typically corresponds to preferred cation-binding sites. Fig. 1a,b shows that both DI and TTE concentrate negative charge on oxygen atoms; however, DI contains three coordinating O atoms and therefore exhibits stronger Na^+ complexation. DI and TTE show ESP_{min} values of −209 and −100 kJ mol^{-1} , respectively, indicating stronger solvation in DI. This trend is also reflected in the computed binding energies (Figure S1b), where DI binds Na^+ more strongly (170 kJ mol^{-1}) than TTE (81 kJ mol^{-1}).

We next experimentally probe how introducing TTE modifies the Na^+ solvation environment. Raman spectra (Fig. 1c) show the characteristic S–N–S stretching region of FSI^- (700–750 cm^{-1}). The FSI^- band shifts to higher wavenumber as solvent solvating power decreases, which is commonly associated with increased populations of CIP and AGG. The observed Raman trend therefore indicates that LHCE exhibits more anion-involved solvation (higher CIP/AGG fraction) than HCE and DE, consistent with prior reports [17].

Small-angle X-ray scattering (SAXS) further reveals the emergence of mesoscale electrolyte nanostructures (Fig. 1d). SAXS probes length scales of ~1–150 nm and is well suited for identifying intermolecular separation, nano-cluster sizes, and domains of structural heterogeneity [18–22]. The corresponding peak positions (q) and D-spacing for each solvent/electrolyte are summarized in Table S1. In NaFSI/DI, two correlation features appear at q = 0.96 $Å^{-1}$ (peak 2, d ~ 6.5 Å) and q = 1.51 $Å^{-1}$ (peak 3, d ~ 4.2 Å), corresponding to local ionic/solvation correlations (e.g. contact-ion pairs) and solvent molecular packing, respectively, consistent with previous SAXS interpretations of concentrated electrolyte [23]. Upon adding TTE, the LHCE SAXS profile changes markedly with the intensity of the peak 2 decreases, and a new peak appears at q = 0.50 $Å^{-1}$ (peak 1, d ~ 12.6 Å). The D-spacing of ~12.6 Å can be assigned as a mesoscale correlation length associated with the spacing between aggregate-rich ionic domains, consistent with TTE-induced nanosegregation and ion-aggregated regions characteristic of LHCE. By comparison, $NaPF_6$/DI (DE) exhibits a broad low-q feature near q ≈ 0.15 $Å^{-1}$ (peak 1, d ~ 62.8 Å), indicating formation of substantially larger and more broadly distributed aggregates in electrolyte environments [24–26].

To directly quantify the Na^+ solvation structure, AIMD simulations were performed (Fig. 1e–g), with a radial cutoff of 3.5 Å defining the first solvation shell. In both HCE and LHCE, the Na^+ solvation shell is primarily composed of oxygen atoms from DI and FSI^-, whereas contributions from TTE oxygen in LHCE are negligible (consistent with TTE acting as a non-solvating diluent). In DE ($NaPF_6$/DI), Na^+ is predominantly coordinated by DI oxygen atoms with minimal direct involvement of PF_6^- in the first shell. Quantitatively, DE shows an average coordination number (CN) of ~ 6 O atoms from DI and negligible PF_6^- contribution (Fig. 1e). In HCE, Na^+ is coordinated by ~ 4 O atoms from DI and ~ 2 O atoms from FSI^- (Fig. 1f). In LHCE, Na^+ exhibits stronger anion involvement, with ~ 2.4 O atoms from FSI^- and ~ 2.3 O atoms from DI, while TTE contributes negligibly to the first solvation shell (Fig. 1g). AIMD snapshots (Fig. 1h–j) further visualize anion-involved clustered motifs in HCE/LHCE, providing an atomistic picture consistent with the aggregate-rich ionic domains inferred from SAXS peak 2 (~6.5 Å) and peak 1 (~12.6 Å) feature upon adding TTE diluent. Thus, AIMD establishes the local (first-shell) coordination environment, while SAXS captures mesoscale organization beyond the first solvation shell; together they provide a consistent multiscale description of LHCE structure.

To further assess the relative reduction susceptibility of species in each electrolyte environment, we computed the projected density of states (PDOS) for DE, HCE, and LHCE (Figure S2). In HCE and LHCE, the conduction band minimum (CBM, analogous to the lowest-lying acceptor states) is predominantly associated with the FSI^- anion, suggesting that initial reduction is more likely to involve anion-derived pathways, which is consistent with the formation of O/F/S-rich

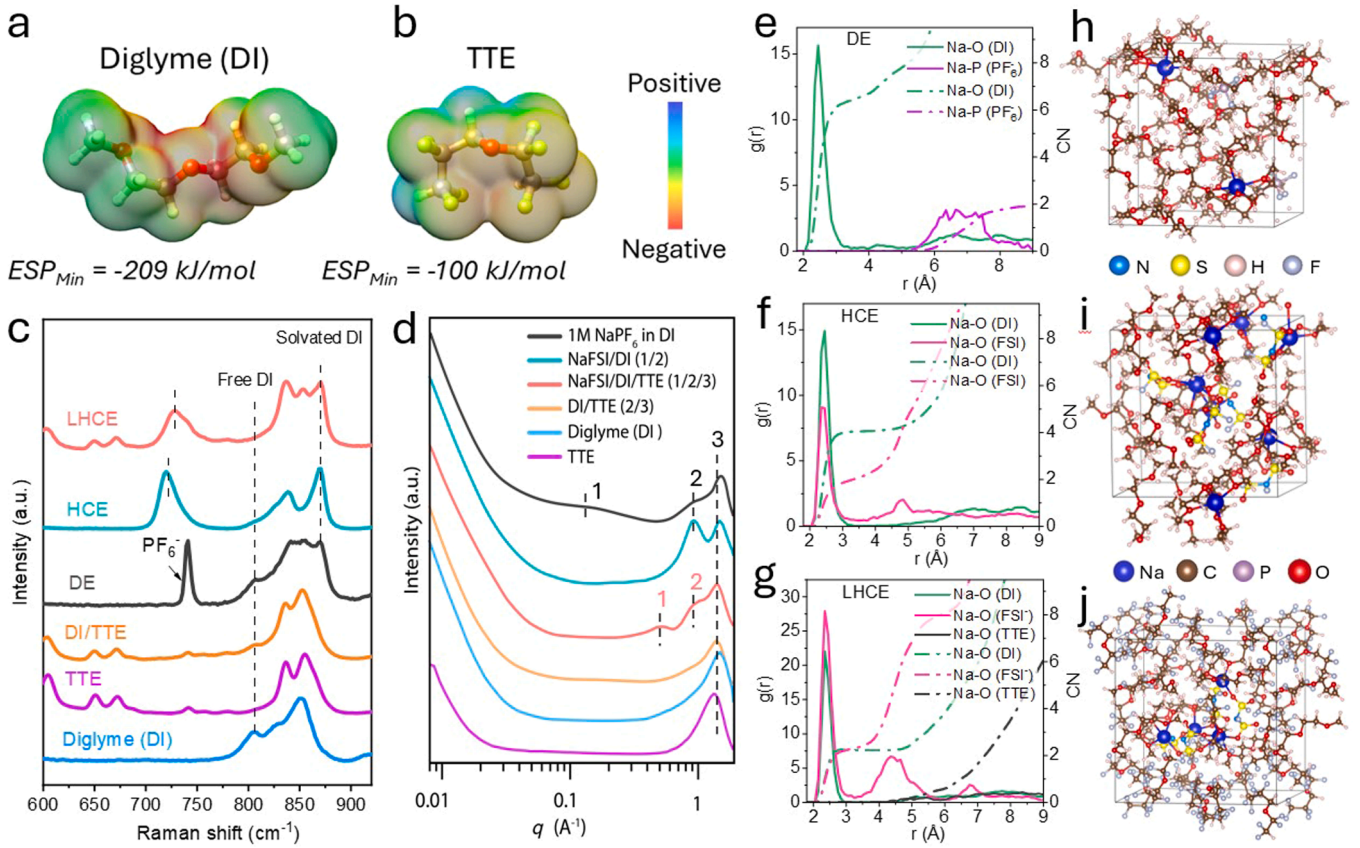

Fig. 1. Solvation-structure characterization of ether-based Na-ion electrolytes. Electrostatic potential (ESP) maps of (a) DI and (b) TTE. (c) Raman spectra highlighting the FSI^- S–N–S stretching region (700–750 cm^{-1}). (d) SAXS profiles of solvents/mixtures and electrolytes showing electrolyte nanostructure evolution upon TTE dilution (Peak 3: solvent packing; Peak 2: local ion/solvation correlations; Peak 1: mesoscale domain correlations). (e–g) AIMD-derived radial distribution functions (RDFs) and coordination numbers (CNs) for (e) DE, (f) HCE, and (g) LHCE (first-shell cutoff: 3.5 Å). (h–j) Representative AIMD snapshots for (h) DE, (i) HCE, and (j) LHCE, illustrating anion-involved coordination and cluster formation. Electrolyte compositions are defined in the Experimental Section.

inorganic SEI components. In contrast, in DE the CBM shows greater contribution from DI-related states, implying a stronger tendency toward solvent-involved reduction and more organic-rich interphase products. Collectively, these DFT and PDOS analyses, together with Raman spectroscopy, SAXS, and AIMD simulation, indicate that introducing TTE preserves a locally concentrated, anion-involved solvation environment characteristic of LHCE, which we next connect to interphase chemistry and full-cell performance.

2.2. *HC|PB full cells performance*

The electrolytes were next evaluated in HC|PB full cells across a wide range of charge/discharge rates to probe kinetic limitations and interphase stability. As shown in Fig. 2a, all three ether-based formulations deliver reversible capacity from 0.1 C to 2 C, but clear differences emerge as the rate increases. DE and HCE show comparable capacity at low rate (0.1 C), whereas HCE maintains higher capacity than DE at elevated rates. Notably, LHCE consistently delivers the highest capacity across the entire rate window (0.1C–2 C), indicating superior rate capability. For comparison, a CBE system (1 M $NaPF_6$ in EC/EMC) exhibits reasonable capacity at low rates but suffers rapid capacity decay at 1C–2 C (Figure S3).

To quantify polarization under operating current, galvanostatic electrochemical impedance spectroscopy (GEIS) was conducted during charging at 50% state of charge (SOC) at 0.33 C (Figure S4a), 1 C (Figure S4b), and 2 C (Fig. 2b). The Nyquist plots were fit using the equivalent circuit shown in the inset of Fig. 2b, and the fitted resistance values are summarized in Table S2. The fitted components include the ohmic resistance (R_b), surface film/interphase resistance (R_{SF}), and charge-transfer resistance (R_{CT}); the depressed semicircle primarily reflects the combined contributions of R_{SF} and R_{CT}. At 0.33 C, the total fitted impedance (R_{SF} + R_{CT}) is lowest for LHCE (91.8 Ω), compared with HCE (139.7 Ω) and DE (178.3 Ω). At 1 C, LHCE remains lower (74.6 Ω) than HCE (123.0 Ω) and DE (230.3 Ω). At 2 C, the impedance gap becomes even larger between LHCE/HCE and DE, with 69.8 Ω (LHCE), 104.8 Ω (HCE), and 300 Ω (DE). These results indicate that LHCE most effectively suppresses polarization growth under high-rate operation. Since GEIS in HC|PB full cells includes overlapping contributions from electrolyte resistance, SEI/CEI, charge transfer, and diffusion, we interpret these results as effective/overall impedance (total polarization) under operating current rather than as a uniquely isolated single-interface resistance. We further evaluated oxidative stability using a leakage-current protocol by charging the full cells to different upper cutoff voltages (3.8, 4.0, 4.1, and 4.2 V vs. Na/Na^+) and holding at each voltage for a fixed time (Fig. 2c). LHCE consistently exhibits lower leakage current than DE, and slightly lower than HCE, especially at higher voltages, indicating improved anodic stability under aggressive conditions and suggesting more stable cathode-side interphase behavior. Long-term cycling was then performed at fixed rates (1.0–3.8 V). At 0.33 C charge/discharge (Fig. 2d), LHCE and HCE show comparable stability, reaching 80% retention after 329 and 344 cycles, respectively, while DE degrades faster. Under a more demanding 1 C protocol (Fig. 2e), the differences become pronounced: DE, HCE, and LHCE reach 80% retention after 87, 446, and 915 cycles, respectively. Representative voltage profiles for DE and HCE at 0.33 C and 1 C are shown in Figure S5. For comparison, the CBE reaches 80% retention after 142 cycles at 1 C (Figure S6a,b). LHCE also maintains excellent stability when the upper cutoff is increased to 4.0 V, retaining 80% capacity after

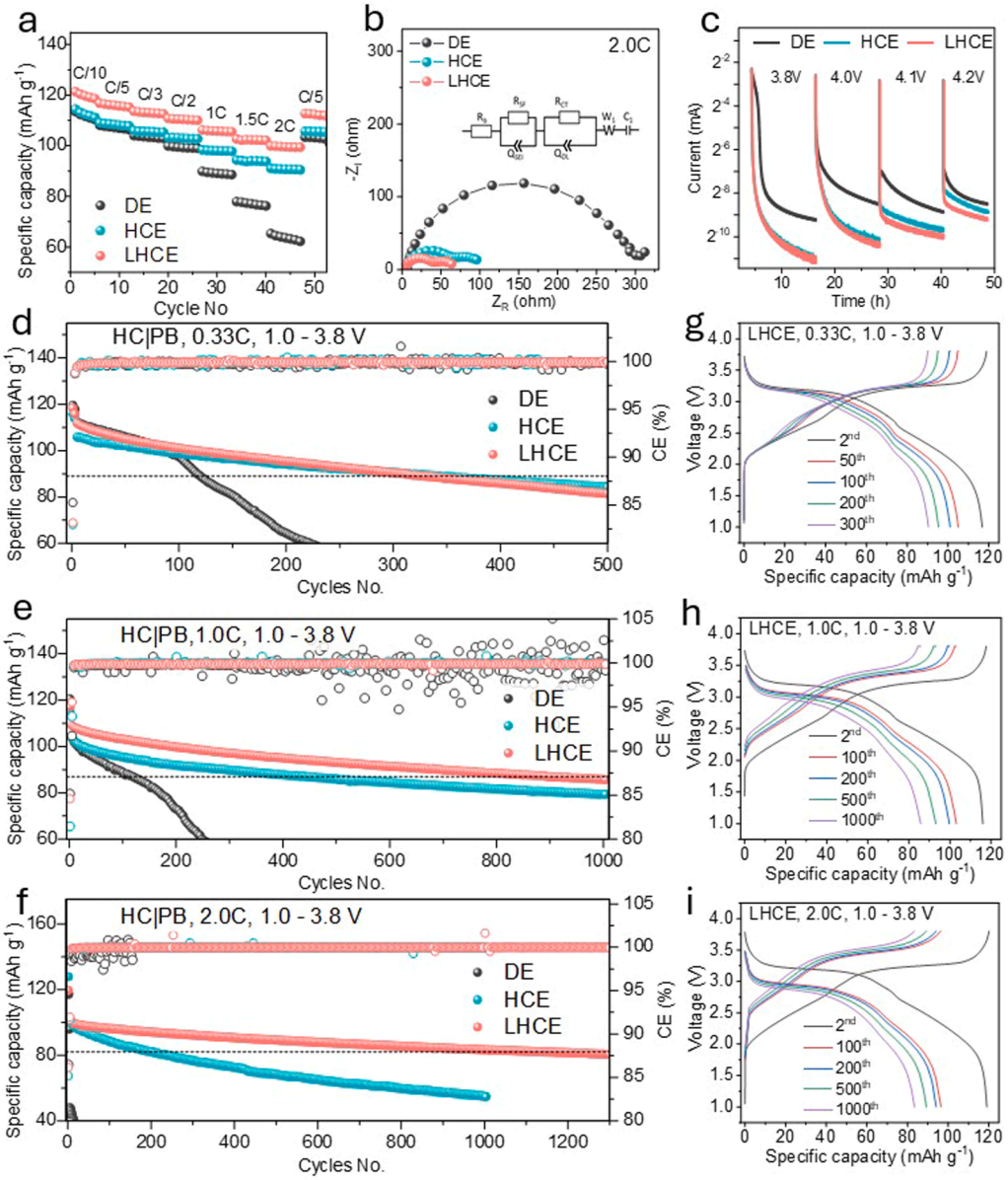

Fig. 2. Electrochemical performance of HC|PB full cells with DE, HCE, and LHCE electrolytes. (a) Rate capability with symmetric charge/discharge C-rates. (b) Galvanostatic electrochemical impedance spectroscopy (GEIS) recorded under 2.0 C charging at 50% state of charge (SOC). Inset shows the equivalent circuit. (c) Leakage current measured after holding fully charged cells at 3.8, 4.0, 4.1, and 4.2 V, respectively. Long-term cycling performance at (d) 0.33 C, (e) 1.0 C, and (f) 2.0 C (charge/discharge), within a 1.0–3.8 V voltage window. (g–i) Representative charge/discharge voltage profiles of LHCE at the indicated C-rates (selected cycles shown).

929 cycles (Figure S6c,d).

At an even higher rate of 2 C charge/discharge (Fig. 2f), LHCE sustains 80% capacity retention for ~1200 cycles, substantially outperforming HCE (~180 cycles). The representative LHCE voltage profiles at different rates are shown in Fig. 2g–i. In contrast, DE exhibits rapid capacity loss at 2 C immediately after the initial formation steps (0.1 C for 2 cycles and 0.33 C for 2 cycles). To place these results in the context of bulk transport, we measured viscosity and ionic conductivity of all electrolytes (Figure S7). Although HCE and LHCE exhibit lower bulk ionic conductivity compared to CBE and DE, they deliver superior rate capability and enhanced-rate cycling stability, indicating that high-rate performance in PB|HC cells is governed not only by bulk conductivity but also by effective interfacial polarization (interphase/charge-transfer contributions). Consistently, HCE/LHCE, especially LHCE, show lower operating impedance at high rates, and form more stable inorganic-rich SEI/CEI, which together mitigate interfacial limitations and suppress total polarization growth under high-rate operation [27].

2.3. *Post-mortem analyses and interphases characterizations*

To understand the interfacial origins of the performance differences, we performed post-mortem analysis of both electrodes and separators after cycling in CBE, DE, HCE, and LHCE electrolytes. Optical images of cycled HC anode, separators, and PB cathodes are shown in Figure S8. For the CBE, the cycled HC anode exhibits localized Na metal plating on the surface, along with a lighter-colored ring near the electrode edge compared to the darker cycling zone. This contrast likely reflects non-uniform deposition of electrolyte decomposition byproducts at the electrode perimeter, as commonly reported for unstable electrolytes under prolonged cycling. Similar edge discoloration is also observed for the DE electrolyte, although without obvious Na metal plating. In contrast, HCE and LHCE show neither pronounced discoloration nor Na

plating on the HC surface, suggesting more stable interphase behavior. Consistently, the separator from CBE and DE cells shows a clear discolored ring and visible deposits in the active region after cycling (CBE showing the most severe yellowish deposition), whereas HCE and LHCE separators show only slight color change with small black powder features even after 1000 cycles. Overall, these visual trends indicate improved interphase stability for HCE and especially LHCE relative to CBE and DE.

2.3.1. HC anode SEI chemistry and thickness

Fig. 3 summarizes the interphase characteristics on the cycled HC anode after 200 cycles at 1 C. In the C 1 s spectra (Fig. 3a), peaks at 284.8 eV (C sp^2), 285.4 eV (C sp^3), 286.6 eV (C–O), and 288.5 eV (C═O) indicate contributions from carbonaceous components and organic/inorganic carbonate-like species [28]. The DE-cycled anode shows slightly higher C–O and C═O intensities than HCE and LHCE, consistent with a more solvent-derived/organic-rich SEI. In addition, the Na–C feature (~283.9 eV), commonly associated with sodiated hard carbon, remains more pronounced for LHCE, suggesting improved reversibility of Na storage under the same cycling protocol. In the F 1 s spectra (Fig. 3b), the LHCE-cycled anode exhibits a stronger Na–F component (~684.0 eV) relative to the C–F component (~687.1 eV) [29], whereas DE shows a weaker Na–F signal and stronger C–F contribution, and HCE lies between these two cases. This trend indicates that LHCE promotes a more inorganic, fluoride-rich SEI. The O 1 s spectra (Fig. 3c) show contributions near ~533 eV (C–O–type species) [30], reflecting organic-dominated SEI components in DE and HCE. HR-TEM further supports that the average SEI thickness is ~30 nm for DE and ~17 nm for LHCE (Figs. 3d and 3e), indicating a thinner, more compact interphase in LHCE. The S 2p spectra of HCE and LHCE (Figure S9a) show deconvoluted peaks at ~162.3 eV (Na_xS), ~167.0 eV (SO_x), and ~170 eV (R–SO_3) [30]. LHCE presents higher intensity of SO_2F, SO_x and Na_xS, whereas HCE shows relatively higher R–SO_3, suggesting a greater anion-derived (salt-derived) contribution in LHCE. In the N 1 s spectra (Figure S9b), the NaN_xO_y peak (~398.4 eV) in LHCE shows higher intensity than the S–N/C–N peak (~400 eV), while HCE is dominated by S–N/C–N, consistent with a more anion-derived SEI in LHCE compared to HCE. Overall, the combined spectral trends indicate that LHCE suppresses excessive solvent-derived decomposition while promoting higher inorganic Na–F/ Na_xS/NaN_xO_y content, consistent with a more passivating SEI. In addition to SEI chemistry, cathode-to-anode crosstalk can accelerate anode degradation and polarization growth. Notably, Fe 2p features (707–715 eV) are detected on the cycled HC anodes (Figure S9c), and the signal intensity follows a clear electrolyte-dependent trend (DE>HCE>LHCE). This trend corresponds with reduced Fe dissolution/migration from the PB cathode and suppressed cross-talk in LHCE, consistent with its improved cathode-side interphase stability during long-term cycling.

To gain additional insight into SEI spatial distribution and composition, ToF-SIMS was performed. The depth profile of DE (Figure S10a) shows both organic fragments (e.g., C_2HO^-) and inorganic fragments (e.g., NaF_2^-) within the SEI, while LHCE (Figure S10b) shows the SEI region enriched in inorganic fragments (e.g., NaF_2^-, NaS^-, NaN_3^- and $NaNSO_2F^-$), consistent with the XPS analysis. The LHCE SEI is also thinner than that of DE. Here, SEI thickness was estimated from the C_2^- (bulk carbon) depth profile as the transition point between the initial rapid rise and the

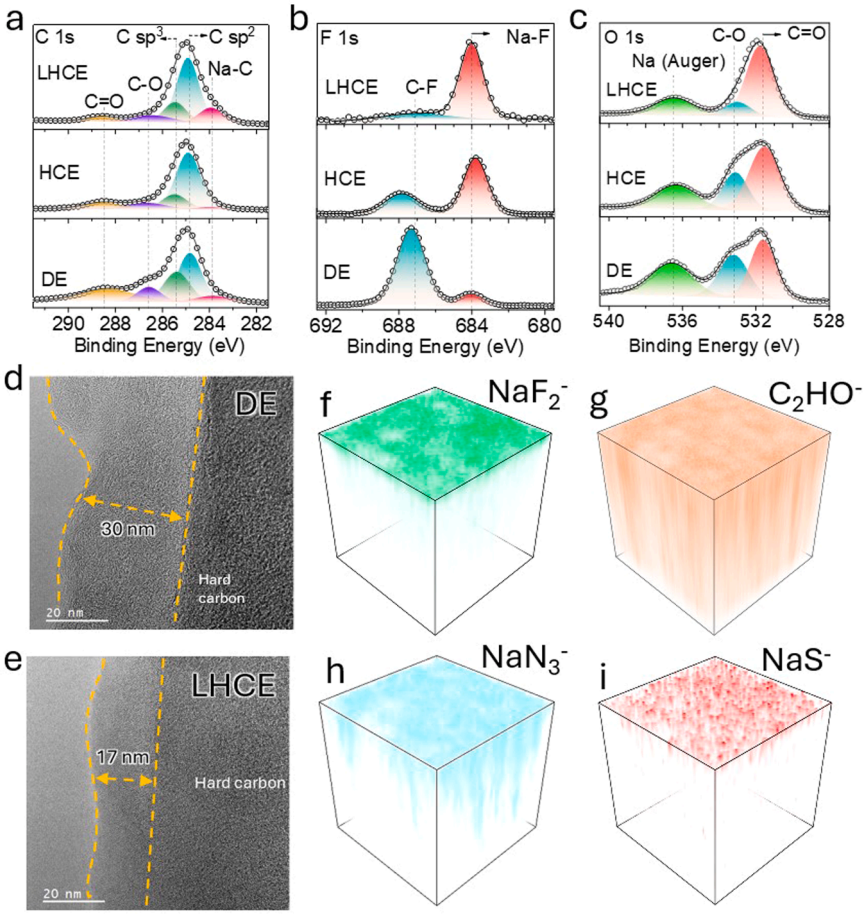

Fig. 3. Post-mortem characterization of cycled HC and SEI. (a-c) X-ray photoelectron spectroscopy (XPS) spectra of cycled HC anode in DE, HCE and LHCE. (d,e) High-resolution TEM (HR-TEM) images of SEI on HC cycled in (d) DE and (e) LHCE. (f-i) ToF-SIMs 3D reconstructions the LHCE-derived SEI using selected secondary ions: (f) NaF_2^-, (g) C_2HO^-, (h) NaN_3^- and (i) NaS^-. All electrodes were harvested from fully discharged cells after 200 cycles at 1 C rate.

subsequent quasi-steady region; the resulting thickness trend agrees with HR-TEM. Three-dimensional ToF-SIMS reconstructions (Fig. 3f–i) further show that representative fragments are distributed relatively uniformly on the anode surface in LHCE, consistent with homogeneous interphase coverage. In contrast, DE (Figure S11) shows a non-uniform distribution of NaF_2 in the SEI, consistent with a more heterogeneous, solvent-derived interphase. Together, XPS, TEM, and ToF-SIMS indicate that LHCE forms a thinner, more inorganic-rich, and more uniform SEI compared with DE and HCE, which is consistent with the reduced polarization and improved high-rate cycling performance discussed above.

2.3.2. PB cathode surface chemistry and morphology

To complement the anode analysis and assess cathode-side stability. Fig. 4 summarizes cathode-side interphase chemistry after 200 cycles at 1 C (XPS) and cathode morphology after 1000 cycles at 1 C (SEM). In F 1 s (Fig. 4a), all electrolytes show a C–F contribution (~688.1 eV), while LHCE exhibits slightly higher NaF enrichment than HCE and DE, consistent with a more inorganic CEI. In N 1 s (Fig. 4b), signals near ~398.3, 400.2, and 402.3 eV correspond to NaN_xO_y/C≡N, S-N/C-N, and Oxidized-N species. LHCE maintains a stronger NaN_xO_y/C≡N contribution relative to S-N/C-N, whereas DE and HCE show a more dominant S-N/C-N feature, suggesting more severe surface degradation/organic fragments in the CEI for those electrolytes.

Fe 2p spectra (Fig. 4c) show contributions from Fe^{2+}–C≡N and Fe^{3+}–C≡N species [13,31]. Compared with LHCE, DE and HCE exhibit higher Fe^{3+}-related intensity, consistent with more oxidative side reactions and/or surface corrosion during cycling. The C 1 s spectra (Figure S12a) further support this trend: LHCE retains a higher C–C/C≡N contribution relative to oxygenated species, whereas DE and HCE show stronger oxygenated carbon components (C–O), consistent with greater electrolyte decomposition on the cathode surface. The O 1 s spectra (Figure S12b) show that the C=O peak (532.5 eV) of DE has higher intensity than HCE and LHCE, indicating a higher fraction of oxidized species. The S 2p spectra (Figure S12c) show that LHCE is dominated by Na_xS (163.8 eV), SO_x (~167.9 eV) and SO_2F (169.0 eV) [30], whereas HCE shows relatively enhanced R-SO_3 (~170.2 eV) compared with LHCE, consistent with a more inorganic CEI in LHCE.

SEM images (Fig. 4d–f) reveal that HCE and LHCE cathodes retain a larger fraction of intact PB cubic crystallites after 1000 cycles, while the DE cathode appears severely de-structured with fewer recognizable cubes. Consistently, the CBE cathode (Figure S13) also shows substantial loss of PB cubic morphology, similar to the DE case. These results indicate that the improved interphase stability in LHCE (and HCE) correlates with better preservation of PB cathode integrity during long-term cycling, reduced cathode dissolution/cross-talk, and improved full-cell durability.

2.4. Pouch-cell performance, gas evolution, and accelerating rate calorimetry

To evaluate practical relevance beyond coin cells, we tested the electrolytes in high-capacity multilayer HC|PB pouch cells and examined cycling stability, gas evolution, and thermal safety. As shown in Fig. 5a, the LHCE pouch cell exhibits excellent durability, retaining 82% capacity after 500 cycles, whereas the DE pouch cell reaches 80% retention after 65 cycles and the CBE pouch cell shows rapid failure within 17 cycles. The corresponding Coulombic efficiencies (Fig. 5b) further highlight the stability of LHCE: LHCE maintains a high and stable CE (~99.3% after 500 cycles), while CBE and DE show pronounced CE fluctuations after only a few cycles, consistent with unstable interphase behavior.

Electrochemical impedance spectra collected after cycling (Fig. 5c) show that LHCE maintains the lowest impedance growth. After 500 cycles, LHCE exhibits a small total fitted impedance ($R_{SF} + R_{CT}$) of ~14 Ω·cm², compared with ~37 Ω·cm² for DE after 65 cycles and ~437 Ω·cm² for CBE after 17 cycles. These results indicate that LHCE suppresses impedance accumulation during long-term cycling, consistent with its improved interphase stability observed in Section 2.3. Gas evolution was quantified after pouch-cell cycling (Fig. 5d and Figure S14a–c). The gas-release volumes for CBE, DE, and LHCE are 107.85 mL/Ah, 6.07 mL/Ah, and 0.26 mL/Ah, respectively. Overall, ether-based DI electrolytes generate substantially less gas than carbonate electrolytes, and LHCE exhibits the lowest gas generation, consistent with reduced continuous parasitic reactions during cycling. While

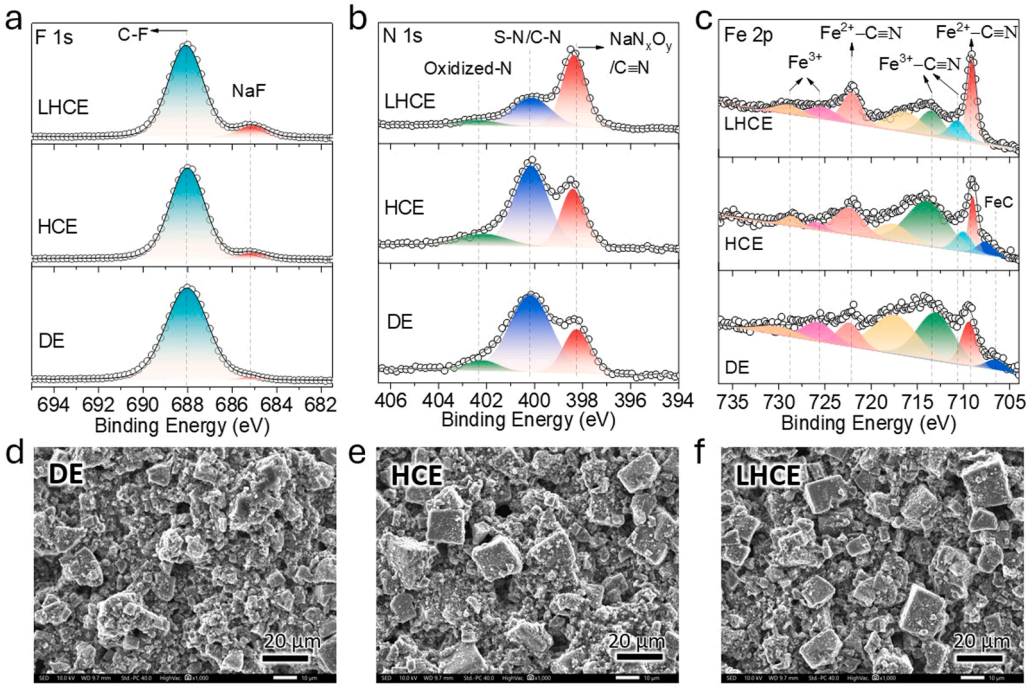

Fig. 4. Post-mortem characterization of cycled PB cathodes. (a-c) XPS spectra of PB cathode harvested after 200 cycles at 1 C in DE, HCE and LHCE. (d-f) SEM images of PB cathode after 1000 cycles at 1 C for different electrolytes.

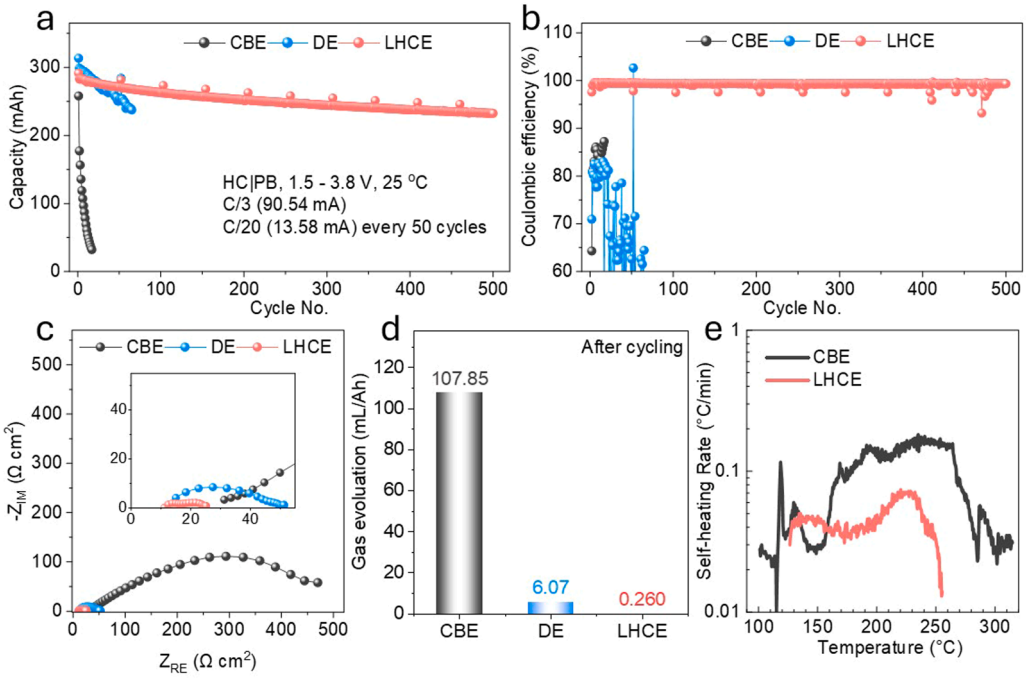

Fig. 5. Pouch-cell performance and safety-related metrics. (a) Cycling performance of HC|PB pouch cells with different electrolytes and (b) corresponding Coulombic efficiencies. (c) Electrochemical impedance spectra and (d) normalized-gas-evolution volume after pouch-cell cycling for CBE (17 cycles), DE (65 cycles), and LHCE (500 cycles). (e) Self-heating rate from accelerating rate calorimetry (ARC) measurements of the 3.8 V charged pouch cells after formation.

HOMO/LUMO calculations provide qualitative insight into oxidative/reductive susceptibility, the suppressed gas evolution in LHCE is most directly attributable to its more stable interphases and reduced ongoing decomposition under cycling conditions.

Post-cycling pouch-cell electrode images provide additional qualitative evidence (Figure S14d,e). In the CBE pouch cell, the HC anode shows clear signatures of Na metal plating, whereas the LHCE anode shows no obvious Na plating even after 500 cycles, consistent with more stable SEI formation and more uniform sodiation/desodiation behavior. Differences in PB cathode appearance between CBE and LHCE are also observed; however, because the cells were cycled for very different durations (17 cycles for CBE vs 500 cycles for LHCE), we avoid excessive interpretation of the cathode color changes. Overall, the rapid failure of CBE pouch cells is most consistent with severe interphase instability (especially on the anode side), as evidenced by Na plating, large impedance growth, and extensive gas release.

Finally, accelerating rate calorimetry (ARC) was used to compare thermal stability between CBE and LHCE pouch cells under a fully charged condition (Fig. 5e). The LHCE-based cell exhibits improved thermal stability, with a delayed exothermic onset temperature of 126.5 °C compared with 101.5 °C for the CBE-based cell. In addition, the self-heating rate of LHCE cells is markedly lower across the measured range, indicating slower thermal runaway progression. Collectively, these pouch-cell results demonstrate that LHCE simultaneously improves cycling stability, gas suppression, and thermal safety, supporting its potential for practical PB-based SIB applications.

3. Conclusion

In this work, we develop a DI/TTE-based localized high-concentration electrolyte (LHCE) for Prussian-blue-based sodium-ion batteries and demonstrate its advantages in both performance and safety. The LHCE design increases anion involvement in the Na^+ solvation environment (higher CIP/AGG fraction), which shifts interphase formation toward more inorganic, FSI-derived species on both the hard carbon anode and the Prussian Blue cathode. As a result, the LHCE suppresses continuous parasitic reactions, mitigates cathode degradation and Fe dissolution/migration to the anode, and enables substantially improved cycling stability from moderate to high rates. Beyond coin-cell metrics, multilayer pouch-cell tests show that LHCE delivers markedly lower gas generation after long-term cycling and improved thermal stability compared with a conventional carbonate-based electrolyte. Overall, tailoring solvation structure through LHCE provides a practical pathway to simultaneously enhance rate capability, cycle life, and safety in Prussian-Blue-based sodium-ion batteries, supporting their viability for real-world applications.

Declaration of Generative AI and AI-assisted technologies in the manuscript preparation process

During the preparation of this work the author(s) used ChatGPT in order to check grammar and spelling. After using this tool, the author(s) reviewed and edited the content as needed and takes full responsibility for the content of the published article.

CRediT authorship contribution statement

P. M.L. Le and **T.-N. Tran** proposed the concept. **T.-N. Tran** designed the experiments and conducted electrochemical measurements, characterizations and data analysis. **V. Shipitsyn** and **L. Ma** performed pouch-cell test, gas release measurements and thermal runaway (ARC) tests. **H.T.D. Nguyen, K. T. Nguyen** and **T. Li** conducted SAXS and Raman measurements. **Y. Xu** and **C. Wang** performed cryo-electron microscopy (cryo-EM) experiments and analysis. **P. Gao** conducted computational simulations and analysis. **Y. Yang** and **B.L. Lucht** performed X-ray photoelectron spectroscopy (XPS) measurements and analysis. **C. Yuan** and **Y. Yao** conducted ToF-SIM and analysis. **K. M. Le** provided optimized HC electrodes. **T.-D. Tran** and **A. L. Phan** assisted with electrochemical experimental setups, analyses, and discussions. All authors discussed the results and contributed to manuscript revisions.

Declaration of Competing Interest

The authors declare that they have no known competing financial interests or personal relationships that could have appeared to influence the work reported in this paper.

Acknowledgements

This work has been supported by the Assistant Secretary for Energy Efficiency and Renewable Energy, Vehicle Technologies Office, of the U. S. Department of Energy (DOE), through the LENS consortium under contract number DE-AC05–76RL01830. Electron microscopy analyses were performed using instrumentation partially funded by a grant from the Washington State Department of Commerce's Clean Energy Fund. Transmission electron microscopy (TEM) was conducted at the William R. Wiley Environmental Molecular Sciences Laboratory (EMSL), a national scientific user facility sponsored by DOE's Office of Biological and Environmental Research located at Pacific Northwest National Laboratory (PNNL). PNNL is operated by Battelle for DOE under Contract No. DE-AC05–76RL01830. Tao Li is thankful for the support from the U.S. National Science Foundation (Grant No. 2342334 and 2323117), Virginia Tech startup funds, and the U.S. Department of Energy (DOE), Vehicle Technologies Office. This research was performed at the Center for Nanoscale Materials and Advanced Photon Source on APS beam time awards (https://doi.org/10.46936/APS-190027/60014116), both U.S. Department of Energy Office of Science User Facilities, was supported by the U.S. DOE, Office of Basic Energy Sciences, under Contract No. DE-AC02–06CH11357.

Appendix A. Supporting information

Supplementary data associated with this article can be found in the online version at doi:10.1016/j.nanoen.2026.111919.

Data availability

Data will be made available on request.

References

[1] B. Zhang, J. Zhang, Y. He, K. Zhou, H. Wang, Recent advances in Prussian blue analogues as cathode materials for sodium-ion batteries, J. Energy Chem. 110 (2025) 593–613, https://doi.org/10.1016/j.jechem.2025.07.010.
[2] M. He, R. Davis, D. Chartouni, M. Johnson, M. Abplanalp, P. Troendle, R.-P. Suetterlin, Assessment of the first commercial Prussian blue based sodium-ion battery, J. Power Sources 548 (2022) 232036, https://doi.org/10.1016/j.jpowsour.2022.232036.
[3] B. Xie, P. Zuo, L. Wang, J. Wang, H. Huo, M. He, J. Shu, H. Li, S. Lou, G. Yin, Achieving long-life Prussian blue analogue cathode for Na-ion batteries via triple-cation lattice substitution and coordinated water capture, Nano Energy 61 (2019) 201–210, https://doi.org/10.1016/j.nanoen.2019.04.059.
[4] M. Jiang, Z. Hou, J. Wang, L. Ren, Y. Zhang, J.G. Wang, Balanced coordination enables low-defect Prussian blue for superfast and ultrastable sodium energy storage, Nano Energy 102 (2022) 107708, https://doi.org/10.1016/j.nanoen.2022.107708.
[5] L. Liu, L. Xiao, Z. Sun, S. Bashir, R. Kasi, Y. Gu, R. Subramaniam, Rational manipulation of electrolyte to induce homogeneous SEI on hard carbon anode for sodium-ion battery, J. Energy Chem. 94 (2024) 414–429, https://doi.org/10.1016/j.jechem.2024.02.055.
[6] J. Peng, W. Zhang, Q. Liu, J. Wang, S. Chou, H. Liu, S. Dou, Prussian blue analogues for sodium-ion batteries: past, present, and future, Adv. Mater. 34 (2022) 1–20, https://doi.org/10.1002/adma.202108384.
[7] P.M.L. Le, T.D. Vo, K.M. Le, T. Tran, Y. Xu, A.L. Phan, L.T.M. Le, H.V. Nguyen, B. Xiao, X. Li, Y. Jin, M.H. Engelhard, P. Gao, C. Wang, J. Zhang, Synergetic dual-additive electrolyte enables highly stable performance in sodium metal batteries, Small 20 (2024), https://doi.org/10.1002/smll.202402256.
[8] Z. Lu, C. Geng, H. Yang, P. He, S. Wu, Q.-H. Yang, H. Zhou, Step-by-step desolvation enables high-rate and ultra-stable sodium storage in hard carbon anodes, Proc. Natl. Acad. Sci. 119 (2022), https://doi.org/10.1073/pnas.2210203119.
[9] K. Sada, S. Nanda, H. Khani, A. Manthiram, Deciphering the local structure of Prussian blue analogue cathodes with Raman spectroscopy for sodium-ion batteries, J. Mater. Chem. A 13 (2025) 22903–22914, https://doi.org/10.1039/D5TA02248G.
[10] J. Zhang, S. Ma, J. Zhang, J. Zhang, X. Wang, L. Wen, G. Tang, M. Hu, E. Wang, W. Chen, Critical review on cathode electrolyte interphase towards stabilization for sodium-ion batteries, Nano Energy 128 (2024) 109814, https://doi.org/10.1016/j.nanoen.2024.109814.
[11] M. Ye, S. You, J. Xiong, Y. Yang, Y. Zhang, C.C. Li, In-situ construction of a NaF-rich cathode–electrolyte interface on Prussian blue toward a 3000-cycle-life sodium-ion battery, Mater. Today Energy 23 (2022) 100898, https://doi.org/10.1016/j.mtener.2021.100898.
[12] X. Huang, X. Chen, Y. Meng, R. Wang, G. Tan, D. Xiao, A superior compatible non-flammable electrolyte to hard carbon anodes for robust sodium ion batteries, N. J. Chem. 48 (2024) 10809–10813, https://doi.org/10.1039/D4NJ01028K.
[13] N. Zhang, L.-Y. Qiu, Y.-S. Zhao, P.-F. Wang, J.-H. Zhang, H. Chang, T.-F. Yi, Design and construction of Prussian blue analogue combined by Na2WO4 toward high-performance cathode materials for Li-ion battery, Appl. Surf. Sci. 629 (2023) 157448, https://doi.org/10.1016/j.apsusc.2023.157448.
[14] Y. Jin, Y. Xu, P.M.L. Le, T.D. Vo, Q. Zhou, X. Qi, M.H. Engelhard, B.E. Matthews, H. Jia, Z. Nie, C. Niu, C. Wang, Y. Hu, H. Pan, J.-G. Zhang, Highly reversible sodium ion batteries enabled by stable electrolyte-electrode interphases, ACS Energy Lett. 5 (2020) 3212–3220, https://doi.org/10.1021/acsenergylett.0c01712.
[15] T. Tran, X. Cao, Y. Xu, P. Gao, H. Zhou, F. Guo, K.S. Han, D. Liu, P.M.L. Le, J. M. Weller, M.H. Engelhard, C. Wang, M.S. Whittingham, W. Xu, J. Zhang, Enhancing cycling stability of lithium metal batteries by a bifunctional fluorinated ether, Adv. Funct. Mater. 34 (2024) 2407012, https://doi.org/10.1002/adfm.202407012.
[16] M. Ghosh, N. Yadav, P. Adelhelm, Glyme-based localized high concentration electrolytes improve the stability of Na-ion battery materials in half-cells, Batter. Supercaps 8 (2025), https://doi.org/10.1002/batt.202400744.
[17] P.C. Rath, Y.W. Wang, J. Patra, B. Umesh, T.J. Yeh, S. Okada, J. Li, J.K. Chang, Composition manipulation of bis(fluorosulfonyl)imide-based ionic liquid electrolyte for high-voltage graphite//LiNi0.5Mn1.5O4 lithium-ion batteries, Chem. Eng. J. 415 (2021) 128904, https://doi.org/10.1016/j.cej.2021.128904.
[18] X. Liu, Z. Yu, E. Sarnello, K. Qian, S. Seifert, R.E. Winans, L. Cheng, T. Li, Microscopic understanding of the ionic networks of "Water-in-Salt" electrolytes, Energy Mater. Adv. 2021 (2021), https://doi.org/10.34133/2021/7368420.
[19] X. Liu, S.-C. Lee, S. Seifer, R.E. Winans, L. Cheng, Y. Z, T. Li, Insight into the nanostructure of "water in salt" solutions: A SAXS/WAXS study on imide-based lithium salts aqueous solutions, Energy Storage Mater. 45 (2022) 696–703, https://doi.org/10.1016/j.ensm.2021.12.016.
[20] H.T.D. Nguyen, S.-C. Lee, X. Lyu, L. Fang, L. Trojanowski, R. Gonzalez, M. Harr, L. Rai, Y. Z, T. Li, Unique conductivity behavior in water-in-salt electrolytes driven by ion clusters, J. Am. Chem. Soc. 147 (2025) 26704–26713, https://doi.org/10.1021/jacs.5c07370.
[21] L. Trojanowski, X. Lyu, S.-C. Lee, S. Seifert, Y. Z, T. Li, Molecular origin of nanoscale anion ordering of LiTFSI electrolytes revealed through SAXS/WAXS and molecular dynamics simulations, ACS Energy Lett. 10 (2025) 696–702, https://doi.org/10.1021/acsenergylett.4c03022.
[22] X. Lyu, H. Wang, X. Liu, L. He, C. Do, S. Seifert, R.E. Winans, L. Cheng, T. Li, Solvation structure of methanol-in-salt electrolyte revealed by small-angle x-ray scattering and simulations, ACS Nano 18 (2024) 7037–7045, https://doi.org/10.1021/acsnano.3c10469.
[23] K. Qian, Z. Yu, Y. Liu, D.J. Gosztola, R.E. Winans, L. Cheng, T. Li, Understanding fluorine-free electrolytes via small-angle X-ray scattering, J. Energy Chem. 70 (2022) 340–346, https://doi.org/10.1016/j.jechem.2022.02.043.
[24] A. Ahmadiparidari, S. Fuladi, L. Majidi, S. Plunkett, E. Sarnello, H. Gholivand, Z. Hemmat, S. Rastegar, S.N. Misal, N. Jimenez, P.C. Redfern, J. Wen, T. Li, A. T. Ngo, F. Khalili-Araghi, L.A. Curtiss, A. Salehi-Khojin, Enhancing the performance of lithium oxygen batteries through combining redox mediating salts with a lithium protecting salt, J. Power Sources 491 (2021) 229506, https://doi.org/10.1016/j.jpowsour.2021.229506.
[25] L. Su, X. Zhao, M. Yi, H. Charalambous, H. Celio, Y. Liu, A. Manthiram, Uncovering the solvation structure of LiPF 6 -based localized saturated electrolytes and their effect on LiNiO 2 -based lithium-metal batteries, Adv. Energy Mater. 12 (2022), https://doi.org/10.1002/aenm.202201911.
[26] K. Qian, S. Seifert, R.E. Winans, T. Li, Understanding solvation behavior of the saturated electrolytes with small/wide-angle x-ray scattering and raman spectroscopy, Energy & Fuels 35 (2021) 19849–19855, https://doi.org/10.1021/acs.energyfuels.1c03328.
[27] I.R. Choi, Y. Chen, A. Shah, J. Florian, C. Serrao, J. Holoubek, H. Lyu, E. Zhang, J. H. Lee, Y. Lin, S.C. Kim, H. Park, P. Zhang, J. Lee, J. Qin, Y. Cui, Z. Bao, Asymmetric ether solvents for high-rate lithium metal batteries, Nat. Energy 10 (2025) 365–379, https://doi.org/10.1038/s41560-025-01716-w.
[28] Thermo Fisher Scientific, Carbon - XPS Reference Table, Thermo Fish. Sci. (n.d.). ⟨https://www.thermofisher.com/us/en/home/materials-science/learning-center/periodic-table/non-metal/carbon.html⟩.
[29] Thermo Fisher Scientific, Fluorine - XPS Reference Table, Thermo Fish. Sci. (n.d.). ⟨https://www.thermofisher.com/us/en/home/materials-science/learning-center/periodic-table/halogen/fluorine.html⟩.
[30] Thermo Fisher Scientific, Oxygen - XPS Reference Table, Thermo Fish. Sci. (n.d.). ⟨https://www.thermofisher.com/us/en/home/materials-science/learning-center/periodic-table/non-metal/oxygen.html⟩.
[31] Thermo Fisher Scientific, Iron - XPS Reference Table, Thermo Fish. Sci. (n.d.). ⟨https://www.thermofisher.com/us/en/home/materials-science/learning-center/periodic-table/transition-metal/iron.html⟩.

Dr. Thanh-Nhan Tran is a Materials Scientist at Pacific Northwest National Laboratory (PNNL). His work spans lithium-metal, silicon-anode Li-ion, and sodium-ion systems, emphasizing long cycle life, fast-charge capability, low gassing, and improved safety in pouch cells. He earned a Ph.D. in Energy Science & Engineering from DGIST (South Korea) and previously held a postdoctoral appointment at Lawrence Berkeley National Laboratory (LBNL). He integrates electrochemistry, materials synthesis, and interphase diagnostics to enable deployable next-generation energy-storage technologies.

Vadim Shipitsyn is a Ph.D. student in Dr. Lin Ma's research laboratory in the Department of Applied Physical Sciences at the University of North Carolina at Chapel Hill. His research focuses on the chemistry of materials and electrolytes for energy storage and conversion systems. He received his Bachelor of Science in Chemical Engineering from the Mendeleev University of Chemical Technology of Russia (MUCTR) and his M. Sc. degree in Materials Science from the Skolkovo Institute of Science and Technology (Skoltech) through a collaboration with Massachusetts Institute of Technology (MIT).

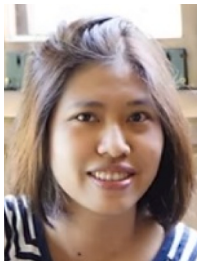

Dr. Huong Nguyen is a Senior Research Associate in the Department of Chemistry at Virginia Tech, working with Prof. Tao Li. Her research focuses on the molecular design and synthesis of advanced electrolyte salts, particularly the fundamental understanding of ion solvation and clustering in battery electrolytes. By integrating synchrotron X-ray scattering, X-ray absorption spectroscopy, and complementary spectroscopic techniques, she reveals nanoscale ion organization and transport mechanisms in complex electrolyte systems. She received her Ph.D. in Chemistry from the University of Science, Vietnam National University - Ho Chi Minh City (VNU-HCM).

Dr. Yaobin Xu is a materials scientist in the Battery Materials and Systems group on the Pacific Northwest National Laboratory (PNNL) campus. He has extensive research experience in the application of novel electron microscopy techniques to advance the fundamental understanding of energy storage materials. Xu has more than 100 papers published in peer-reviewed professional journals, including Science, Nature Review Materials, Nature Energy, Nature Nanotechnology, Nature Catalysis, et al. He obtained a Ph.D. in material physics and chemistry from the Institute of Metal Research, Chinese Academy of Sciences, in 2016.

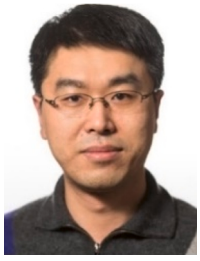

Dr. Peiyuan Gao is a Mathematician in Physical & Computation Science Directorate at Pacific Northwest National Laboratory (PNNL). He joined PNNL in 2016. His current research interests focus on multiscale modeling and simulation of polymers and batteries and scientific AI/ML model development for material property prediction and design. He has published more than 70 peer-reviewed journal papers in leading journals such as Nat. Energy, Angew. Chem. Int. Ed, and PNAS. He obtained Ph.D. in Chemistry from the Institute of Chemistry, Chinese Academy of Sciences.

Dr. Yuxin Yang is a postdoctoral research fellow at the University of Rhode Island (URI). He joined URI in 2025 and currently researches electrolyte additives for high-energy-density lithium- and sodium-ion batteries. His work integrates organic synthesis, electrochemical characterization, and post-cycling analysis of batteries. He received his B.Sc. from Beijing Institute of Technology and Ph.D. from Clark University. His Ph.D. research focused on developing single-ion conducting polymer electrolytes for solid-state lithium-metal batteries.

Changyu Yuan is a Ph.D. student at the University of Houston. His research focuses on understanding the anode–electrolyte interphase and developing electrolyte design strategies for sodium-ion batteries.

Khanh T. Nguyen obtained a bachelor's degree in Department of Chemistry from Ho Chi Minh City University of Education (Ho Chi Minh City, Viet Nam) in 2024. Currently, he is Ph.D. student under the guidance of Prof. Tao Li at Virginia Tech. His research focuses on the electrolyte structure, improving battery performance, and investigating the electrochemical properties of liquid electrolytes in lithium-based batteries using synchrotron-based techniques.

Kha Le is a Materials Scientist at Pacific Northwest National Laboratory (PNNL) and a Ph.D. student in Mechanical Engineering at the University of Washington. His research focuses on electrolyte design and advanced anode materials for beyond lithium-ion battery systems. He works on lithium-ion, lithium-sulfur, and sodium-ion batteries with the goal of improving cycle life, increasing energy density, and reducing cost by using earth-abundant materials. His work combines electrochemistry, materials synthesis, and advanced characterization techniques to understand interphase formation and electrode heterostructures, enabling scalable next-generation energy storage technologies.

Thuy-Dung Tran is an electrochemistry technician at Pacific Northwest National Laboratory (PNNL), specializing in battery materials, cell assembly, and electrochemical testing for Na-ion, Li metal, and Li-ion batteries. She earned a M.Sc. degree in Department of Chemistry at the University of Science, VNU HCM (Vietnam). Her interests include electrochemistry, interphase chemistry, and the synthesis of materials for energy conversion and storage systems.

Dr. An L. Phan is a Postdoctoral Associate at Pacific Northwest National Laboratory (PNNL). He received his Ph.D. in Chemical Engineering under the supervision of Prof. Chunsheng Wang at the University of Maryland. His research focuses on electrolyte design for next-generation lithium- and sodium-based batteries, with particular emphasis on high-energy chemistries such as metal and alloy anodes, high-voltage cathodes, and sulfur-based cathodes. His work explores new electrolyte concepts and interfacial phenomena to advance cell-level energy density, cycle life, safety, and cost.

Dr. Brett L. Lucht is a Full Professor at the University of Rhode Island, specializing in organic and materials chemistry. His research focuses on the development of innovative electrolytes for lithium-ion batteries, specifically for electric car applications. His team explores novel salts, solvents, and additives to enhance battery performance, safety, and stability across extensive temperature and voltage ranges. Current research objectives encompass prolonging battery lifespan, improving high-capacity and high-voltage electrodes, and formulating non-flammable electrolytes. He obtained his Bachelor of Science in Chemistry from the University of Puget Sound and his Doctorate in Organic Chemistry from Cornell University.

Dr. Yan Yao is a Distinguished Professor in University of Houston. His research integrates electrochemistry and materials science, with a focus on multivalent, solid-state, and aqueous batteries that improve safety and sustainability. He serves as Thrust Co-Lead in DOE's Energy Storage Research Alliance and leads major battery initiatives, including Battery500, LENS, and multiple ARPA-E projects. Dr. Yao has authored over 150 papers, holds 12 U.S. patents, co-founded two start-ups, and has received numerous honors, including the 2025 Edith and Peter O'Donnell Award in Engineering.

Dr. Tao Li is a Full Professor in Virginia Tech's Department of Chemistry with a joint appointment at Argonne National Laboratory. His research focuses on materials for energy conversion and storage, especially next-generation batteries, electrolytes, and catalysts, using advanced synchrotron X-ray characterization to understand structure and performance. His work spans liquid, molten-salt, and solid-state electrolytes, as well as catalysts for electrochemical reactions such as CO_2 reduction and oxygen reduction.

Dr. Chongmin Wang is a Laboratory Fellow at Pacific Northwest National Laboratory (PNNL). He received his B.Sc. and M. Sc. in physics from Lanzhou University (China) and Ph.D. in Materials Science and Engineering from University of Leeds (UK). Before joining PNNL, he worked at the Max Planck Institute for Metals Research (Germany), NIMS (Japan), and Lehigh University. His research focuses on advanced microscopy, specifically in situ microscopy and energy materials. He has received numerous honors. He currently serves as the principal editor of JMR and is a Fellow of the Materials Research Society, and Fellow of Microscopy Society of America.

Dr. Lin Ma is an Assistant Professor at University of North Carolina at Chapel Hill. He leads the Electrochemical Energy Storage and Conversion Group, developing next-generation rechargeable batteries through materials science and electrochemical engineering. He has authored more than 90 peer-reviewed publications. Since founding the group in 2022, he has driven impactful research on cathode materials and electrolytes for metal-ion batteries while supervising students who have gone on to successful industry careers. He now continues to develop safer, lower-cost, fast-charging battery technologies with higher energy density and longer lifetimes.

Dr. Phung Le is a Senior Scientist in Battery Materials Research within the Energy & Environment Directorate at Pacific Northwest National Laboratory (PNNL), where she leads DOE-VTO-funded efforts including LENS and Batt500 on electrolyte development. She is also an Adjunct Associate Professor at the University of Science, VNU-HCM, Vietnam, and an Affiliate Professor in Materials Science and Engineering at the University of Washington. Her research focuses on designing materials for energy conversion and storage, with deep expertise in electrochemistry and the physical chemistry of liquid electrolytes, including ionic liquids.